batteries

Article

Optimization of Lithium Metal Anode Performance: Investigating the Interfacial Dynamics and Reductive Mechanism of Asymmetric Sulfonylimide Salts

Shuang Feng [1], Tianxiu Yin [1], Letao Bian [1], Yue Liu [1,*] and Tao Cheng [1,2,*]

[1] Institute of Functional Nano & Soft Materials (FUNSOM), Jiangsu Key Laboratory for Carbon-Based Functional Materials & Devices, Joint International Research Laboratory of Carbon-Based Functional Materials and Devices, Soochow University, 199 Ren'ai Road, Suzhou 215123, China; sfengsfeng@stu.suda.edu.cn (S.F.); txyin@stu.suda.edu.cn (T.Y.); ltbian@stu.suda.edu.cn (L.B.)
[2] Jiangsu Key Laboratory of Advanced Negative Carbon Technologies, Soochow University, Suzhou 215123, China
* Correspondence: yliu1992@suda.edu.cn (Y.L.); tcheng@suda.edu.cn (T.C.)

Abstract: Asymmetric lithium salts, such as lithium (difluoromethanesulfonyl)(trifluoromethanesulfonyl) imide (LiDFTFSI), have been demonstrated to surpass traditional symmetric lithium salts with improved Li^+ conductivity and the capacity to generate a stable solid electrolyte interphase (SEI) while maintaining compatibility with an aluminum (Al^0) current collector. However, the intrinsic reductive mechanism through which LiDFTFSI influences battery performance remains unclear and under debate. Herein, detailed SEI reactions of LiDFTFSI–based electrolytes were investigated by combining density functional theory and molecular dynamics, aiming to clarify the formation process and atomic structure of the SEI. Our results show that asymmetric $DFTFSI^-$ weakens the interaction between carbonate solvents and Li^+, and substantially alters the solvation structure, exhibiting a well-balanced coordination capacity compared to bis(trifluoromethanesulfonyl)imide ($TFSI^-$). Nanosecond hybrid molecular dynamics simulation further reveals that preferential decomposition of LiDFTFSI produces sufficient LiF and Li_2O to facilitate a robust SEI. Moreover, abundant F^- generated from LiDFTFSI decomposition accumulates on the Al surface and subsequently combines with Al^{3+} from the current collector to form AlF_3, potentially inhibiting corrosion of the current collector. Overall, these findings elucidate how LiDFTFSI regulates the solvation sheath and SEI structure, advancing the development of high-performance electrolytes compatible with current collectors.

Keywords: lithium metal battery; electrolyte solvation structure; battery interphase; LiDFTFSI; hybrid molecular dynamics

Citation: Feng, S.; Yin, T.; Bian, L.; Liu, Y.; Cheng, T. Optimization of Lithium Metal Anode Performance: Investigating the Interfacial Dynamics and Reductive Mechanism of Asymmetric Sulfonylimide Salts. *Batteries* **2024**, *10*, 180. https://doi.org/10.3390/batteries10060180

Academic Editor: Marco Giorgetti

Received: 18 April 2024
Revised: 20 May 2024
Accepted: 21 May 2024
Published: 24 May 2024

1. Introduction

As the demand for sustainable energy storage grows, developing and innovating high-energy-density batteries has become one of the most important research areas in the field of energy storage and a driving force behind the development of new energy sources [1–4]. Lithium-ion batteries (LIBs), which currently have the largest market share, consist of electrodes (an anode and a cathode), an electrolyte, separator, and current collectors, each crucial for battery performance. Recent advances in electrode materials have improved battery capacity and lifespan due to atomic-based simulations of electronic structures. Kothalawala et al.'s work on $LiNiO_2$ cathodes exemplifies these advancements [5,6]. Recent multiscale simulations have also enhanced our understanding of battery electrolytes by clarifying reduction product aggregation near electrodes and affecting SEI morphology [7]. These techniques provide insights into electrolyte structures, solvation environments, and interfacial reactions in lithium-based batteries [8], and reveal the complex interplay in lithium–sulfur batteries [9]. These advancements underscore the importance of multiscale simulations in improving battery performance and design.

Lithium metal batteries (LMBs), which serve as the most promising next-generation energy storage devices due to their ultra-high battery capacity and compatibility with existing battery manufacturing equipment, have currently been drawing significant research interests all around the world. LMBs possess a specific capacity of 3860 mAh g^{-1} and a low electrochemical potential of −3.04 V (vs. a standard hydrogen electrode, SHE), showing advantages in terms of energy density compared to those of LIBs [10–15]. However, LMBs face significant challenges, such as the uncontrollable growth of lithium dendrites and the formation of an unstable solid electrolyte interphase (SEI) during charge–discharge cycles. These issues can be attributed to the high reactivity of lithium metal and inevitable side reactions between the electrolyte and the anode [16–20], which compromise the cycle life and performance of LMBs and, more critically, pose serious safety issues during use [21]. To address these concerns, significant efforts have been devoted to designing advanced lithium anode structures [22–24], constructing artificial SEIs [25,26], and optimizing electrolytes [27,28]. Among various strategies, electrolyte engineering is one of the most effective and feasible approaches for regulating the homogenous and stable formation of an SEI. Electrolyte engineering mainly includes (1) adjusting the electrolyte formula based on the existing components, such as by using high-concentration electrolytes or additives, and (2) molecular design based on existing electrolyte components. Increasing salt concentrations facilitates the sacrificial reduction of anions and limits coordination of the solvent with lithium ions (Li^+), thus enabling inorganic-dominated SEI growth [29,30]. LiF is crucial for forming highly stable SEIs, prompting the introduction of various fluorine-containing components to increase its content. For example, 1,4-dimethoxybutane [31] promotes both ionic conductivity and enriched LiF formation in the SEI, thus inhibiting Li dendrite growth by facilitating uniform Li deposition [32]. Furthermore, additives (fluoroethylene carbonate [33,34], $LiNO_3$ [35,36], and saccharin sodium [37]) enhance the stable formation of SEIs by accelerating decomposition and reducing side reactions between other electrolyte components and the electrode, thereby improving battery performance. The SEI predominantly forms on the electrode surface due to electrochemical reactions occurring during the initial charging cycles. While the SEI primarily forms on the electrode, it can also extend to the current collector, especially under high voltages or elevated temperatures, due to the electrolyte permeating throughout the cell, and typically the SEI is thinner and less uniform than on the electrode surface [38].

Various electrolytes exist, but lithium salts in LMBs are notably limited. Lithium hexafluorophosphate ($LiPF_6$) is widely used commercially owing to its good performance and affordable price. $LiPF_6$ features a suitable Li^+ transportation property, along with an effective passivation effect on the Al^0 current collector by generating AlF_3. The band-gap of aluminum fluoride (AlF_3) is approximately 14 eV, as indicated in a study [39]. This high band-gap value is similar to that of LiF, making AlF_3 an insulator. However, the chemical and thermodynamic stability of $LiPF_6$, especially toward Li^0, is insufficient. PF_6^- rapidly decomposes at elevated temperatures and is hydrolytically sensitive, limiting its use in advanced batteries [40]. Alternatives to $LiPF_6$, like LiBOB and LiDFOB, offer better thermal stability and can passivate Al foil, yet their low conductivity and solubility fail to satisfy battery system requirements [41]. Lithium salts like LiTFSI, with high charge delocalization, improve conductivity and SEI uniformity but severely corrode the Al^0 current collector. Recently, Zhang et al. developed a novel asymmetric lithium salt, lithium (difluoromethanesulfonyl)(trifluoromethanesulfonyl)imide (LiDFTFSI), aiming to counteract the shuttling effect of polysulfide intermediates in lithium–sulfur batteries through anion modification [42]. Altering the $–CF_3$ group to the weaker acidic $–CF_2H$ group enhances Li^+ conductivity by limiting anionic mobility through hydrogen bonding and promotes stable SEI formation via enhanced anion reduction. More importantly, this straightforward modification of disrupting functional group symmetry substantially improves compatibility with the Al^0 current collector. Qiao et al. proposed that the formation of sufficient AlF_3 from an LiDFTFSI–based electrolyte can passivate Al foil even at 4.2 V (vs Li/Li^+), which explains its greater compatibility with the Al^0 current collector compared to

LiTFSI [43]. Nevertheless, the underlying reductive reactions of $DFTFSI^-$, SEI formation, and collector passivation mechanisms remain unclear. Elucidating elementary reaction mechanisms helps to establish design criteria from a chemical perspective, enabling rational electrolyte design.

In this work, we employed multiscale simulations to investigate the physical and chemical properties of electrolytes and underlying reaction mechanisms, which provided insights into SEI formation and its structural evolution. Specifically, the unique solvation structure of $DFTFSI^-$ and Li^+ was studied and compared with that of carbonate solvents in an electrolyte. To study electrolyte reduction and the SEI formation mechanism, the hybrid ab initio and reactive force field molecular dynamics (HAIR) method was employed to improve computing efficiency while retaining accuracy. Quantum mechanical (QM) calculations are accurate and transferable but expensive. Force-field-based calculations, such as ReaxFF, are much faster but less accurate, though sufficient for mass transfer. Combining QM and ReaxFF accelerates simulations by 10 to 100 times with minimal loss of accuracy. This reduces months-long calculations to days, making them more feasible. Importantly, our simulations have shown that deep reactions within the battery interphase are crucial for performance regulation and can only be captured by longer simulations, beyond the scope of short AIMD simulations [44]. To compare the electrolyte decomposition products with the experimental results, an X-ray photoelectron spectroscopy (XPS) simulation of the SEI structure was performed. Additionally, we explored the passivation mechanism of $DFTFSI^-$ on the Al^0 current collector using accurate density functional theory (DFT) calculations to elucidate the thermodynamic reductions of $DFTFSI^-$ and $TFSI^-$ on the Al electrode. This study not only bridges the knowledge gap regarding LiDFTFSI behavior at the atomic level but also offers new perspectives for designing innovative lithium salts to advance the commercialization of LMBs.

2. Computational Details

2.1. Classical Molecular Dynamics (cMD) Simulations

cMD simulations were carried out using GROMACS (version 2020.3) [45] to simulate bulk electrolytes. The workflow was as follows: First, model optimization was performed, followed by a 2 ns canonical (NVT) simulation at 300 K. Subsequently, a 2 ns isothermal–isobaric (NPT) simulation was conducted at 300 K and 1.0 bar pressure using a Nosé–Hoover thermostat. After reaching equilibrium, a final 2 ns NVT simulation was carried out. Additionally, a custom code was utilized to extract and statistically analyze the coordination, with a cutoff radius of 2.7 Å used to determine the coordination of Li^+ with anions or solvent molecules.

Based on the experimental electrolyte formula (1 M LiDFTFSI in a mixture of ethylene carbonate (EC) and ethyl methyl carbonate (EMC)), a simulation box with a size of $4 \times 4 \times 4$ nm^3 was built, consisting of 40 Li^+, 40 $DFTFSI^-$, 160 EC, and 240 EMC. To compare, the 1 M LiTFSI EC/EMC electrolyte, a simulation was built with a box size of $4 \times 4 \times 4$ nm^3, consisting of 40 Li^+, 40 $TFSI^-$, 160 EC, and 240 EMC.

2.2. AIMD and RMD Simulations

The AIMD simulation was carried out using VASP (version 5.4.4) with the Projected Augmented Wave (PAW) method [46] and a plane-wave basis set. The method was density functional theory (DFT) with generalized gradient approximations (GGA) of the Perdew–Burke–Ernzerhof (PBE) functional [47]. The energy cutoff for the plane-wave basis expansion was set at 400 eV, and the convergence threshold energy for the self-consistent calculation and geometry relaxation was less than 1×10^{-5} eV. These MD simulations used only the gamma point of the Brillouin zone with no consideration of symmetry. A dispersion correction, the DFT-D3 method with Becke–Johnson damping [48], was included in the calculations. The RMD simulation was carried out using LAMMPS (version 12, December 2018). The time step for the RMD simulation was set to 0.25 fs, and the NVT ensemble simulation was conducted at 300 K.

The workflow was as follows: First, a 50 ps AIMD simulation explored initial chemical reactions in the electrolyte system. This was followed by a HAIR simulation alternating between 0.5 ps AIMD and 10-fold-accelerated RMD simulations. As electrochemical reactions decreased and mass transport dominated, a 100-fold acceleration was used to study deeper reactions, extending the simulation beyond 2.5 ns. To reach equilibrium, high-precision AIMD was used to obtain reliable SEIs and products, providing accurate data for XPS simulations. A diagram of the workflow is shown in Figure S1.

To investigate electrolyte decomposition, the box size was set to $10.5 \times 10.5 \times 26.5$ Å^3, consisting of one LiDFTFSI, four EC, and six EMC. Six layers (3×3) of Li (100) were set at the bottom of the box to simulate a Li anode. During the simulation, the bottom two layers were fixed to represent the bulk anode. To relax this electrolyte/anode interface, geometry optimization was carried out, as shown in Figure S2.

3. Results and Discussion

3.1. Electrolyte Solvation Structure Analysis

cMD simulations were carried out to investigate the specified solvation structure of the LiDFTFSI-EC/EMC electrolyte caused by the asymmetric structure. The solvation structure of an electrolyte is determined by its molecular structure, which can be distinguished into three categories [32,49]: (1) solvents surrounding Li^+ (SSL), (2) Li^+–anion single pairs (LASPs), and (3) Li^+–anion clusters (LACs). A strong Li^+–solvent interaction should be avoided as it inhibits desolvation and triggers solvent cointercalation during Li^+ reduction while charging [50]. Comparisons of solvation structures between LiDFTFSI and LiTFSI are as shown in Figure 1a and Figure S3a. Based on Li^+ coordination with oxygen, the proportions of SSL, LASP, and LAC in the LiDFTFSI system are 35%, 27.5%, and 37.5%, respectively, while in the LiTFSI system, these are 47.5%, 27.5%, and 25%, respectively. Thus, the proportion of SSL in the LiDFTFSI system is much lower than that in the LiTFSI system. The significant increase in the proportion of LAC solvation structures suggests a shift in the solvation structure from SSL to LASP and LAC.

In the LiDFTFSI system, a greater number of anions penetrate the solvation sheath and contribute to the first solvation sheath of Li^+. To understand such an effect, DFT calculations were used to obtain the electrostatic potential (ESP) energy surface of $TFSI^-$ and $DFTFSI^-$, which showed that the ($–CF_2H$) substituent of $DFTFSI^-$ differs significantly from the ($–CF_3$) substituent of $TFSI^-$, resulting in $–CF_2H$ having a less negative charge, while the O on the S connected to $–CF_2H$ has a greater electron density, indicating that O has a stronger electrostatic interaction with Li^+ during coordination (Figure S3b). Meanwhile, $DFTFSI^-$ facilitates hydrogen bonds with solvent molecules, in turn enhancing ionic conductivity. A considerable amount of $DFTFSI^-$ enters the first solvation sheath, displacing solvent molecules and enriching the solvation structure with $DFTFSI^-$. Table S1 provides additional statistics on Li^+ coordination. Compared to the LiTFSI system, the LiDFTFSI system exhibits a higher average anion coordination number and a lower average solvent coordination number. This anion-rich solvation structure can facilitate preferential salt decomposition, resulting in the formation of an inorganic-rich SEI interface.

The radial distribution function (RDF) and coordination numbers (CNs) provide further insights into the detailed structural features of anions and solvent molecules within the solvation sheath in both systems (Figure 1b,c). As shown in Figure 1b, in the LiDFTFSI system, the RDF peaks of Li^+–O of $DFTFSI^-$, EC, and EMC are located at 0.208, 0.216, and 0.212 nm, respectively, indicating that $DFTFSI^-$ penetrates into the first solvation sheath. The corresponding CN values are 1.05, 1.73, and 2.51, respectively. The CN of Li^+-O($DFTFSI^-$) (1.05) is significantly greater than that of Li^+–O($TFSI^-$) (0.88), while the CN of Li^+–O(EC) (1.73) decreases in the LiDFTFSI system, indicating that $DFTFSI^-$ weakens the interaction between EC and Li^+. Additionally, the binding energy between $DFTFSI^-$ and Li^+ is -1.34 eV (Figure 1d), further showing that $DFTFSI^-$ strongly coordinates with Li^+ and enters the solvation sheath, thereby modifying the solvation structure, consistent with a previous report [51].

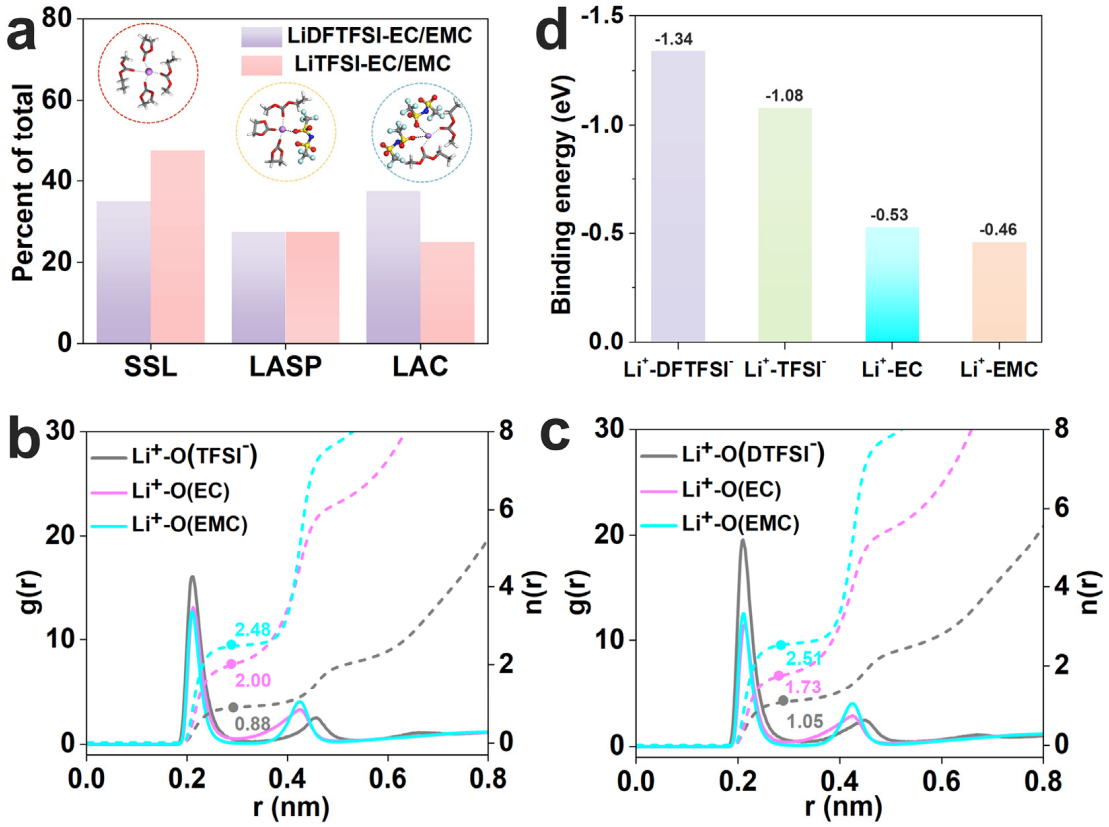

Figure 1. (**a**) Statistical diagrams of the proportion of solvation structures after cMD simulation and examples of three solvation structures of the LiDFTFSI-EC/EMC electrolyte. Color codes: lithium: purple, oxygen: red, carbon: gray, fluorine: cyan, sulfur: yellow, nitrogen: blue, and hydrogen: white. RDF (solid lines), g(r) and CN (broken lines), and n(r) of Li^+–O in the LiDFTFSI system (**b**), and LiTFSI system (**c**). (**d**) The binding energies between lithium ions and different species.

3.2. The Underlying Mechanism of Electrolyte Reduction and SEI Formation

Hybrid molecular dynamics simulations were carried out to investigate the decomposition and initial SEI formation of the LiDFTFSI-EC/EMC electrolyte. Electrolyte reduction is crucial for SEI formation at the lithium metal anode. According to reports, during the decomposition process, with the cleavage of the S–N bond, the symmetric lithium salt LiTFSI decomposes into two groups and produces LiF, which facilitates the formation of a thin and dense SEI. A 2.86 ns HAIR simulation using the model shown in Figure S2b reveals the detailed SEI reaction of the LiDFTFSI electrolyte. As shown in Figure 2, $DFTFSI^-$ basically decomposed within 7 ps in the AIMD simulation. The detailed reactions are as follows: The N–S bond on the $–CF_2H$ side breaks at 0.19 ps, followed by the rapid cleavage of the C–F bonds on $–CF_2H$ at 1.21 ps due to the formation of LiF, reduced by Li^0. The S–O bond breaks at 1.51 ps, along with Li_2O formation (Figure 2a). Only in the extended simulation can the dehydrogenation reaction be observed (72.60 ps). Our calculations show that the formation of LiH is inevitable but much slower than LiF in the case of $DFTFSI^-$, which is consistent with previous experimental results.

On the other hand, the $–CF_3$ group detached from the salt at 3.20 ps through C–S bond cleavage, similar to a previous report [44]. Further reduction of $DFTFSI^-$, followed by S–O, N–S, and C–F cleavages, contributed to the inorganic components of the SEI (Figure 2b). Breaking of the N–S bond occurred at 5.26 ps, and all F atoms were released from $DFTFSI^-$ at 6.88 ps (Figure 2b). The results show that the $–CF_3$ group decomposes later than $–CF_2H$, indicating that the introduction of the asymmetric substitution of H atoms further enhances the reactivity of $–CF_2H$. This detailed mechanism demonstrated that asymmetric $DFTFSI^-$ can rapidly react with Li^0 and generate products, including LiF, Li_2O, and Li_3N, which can

potentially improve ionic conductivity, regulate the mechanical properties of the SEI, and inhibit dendrite formation [11]. The decomposition mechanism of $DFTFSI^-$ revealed by the AIMD simulation supports the experimental hypothesis, as illustrated in Figures 2c and S4.

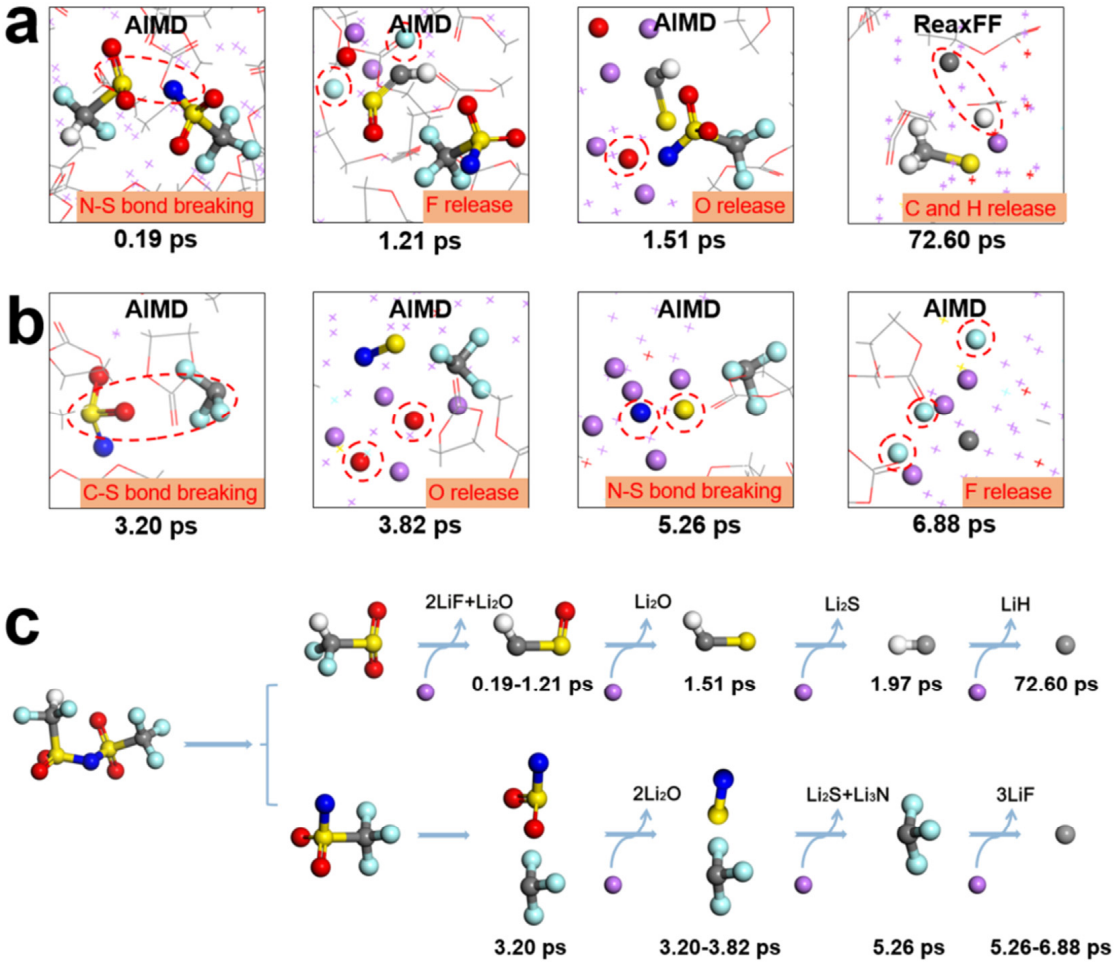

Figure 2. Sequence of $DFTFSI^-$ decompositions obtained from AIMD and HAIR simulations for the 1 M LiDFTFSI-EC/EMC system. (**a**) Decompositions of the side of the $–CF_2H$ group. (**b**) Decompositions of the side of the $–CF_3$ group. (**c**) $DFTFSI^-$ reaction pathway obtained from simulations. The color codes are the same as those in Figure 1a.

The solvent decomposition mechanism is crucial. AIMD simulations indicate that EC is reduced during charging, contributing to SEI formation. EC starts to decompose within 50 ps, and three different initial pathways can be distinguished based on the reactive trajectories. At 2.51 ps, in a Li^+-rich environment, EC undergoes a one-electron reduction, breaking its C–O bond and transforming from a ring to a chain structure, forming $OC_2H_4OCO^-$. Subsequently, $OC_2H_4OCO^-$ follows two pathways: It accepts another electron to form $OC_2H_4O_2{}^-$, releasing one CO at 4.00 ps (Figure 3a), and releases CO_2 while forming the free radical anion $\bullet C_2H_4O^-$, consistent with previous DFT calculations [52]. At 61.21 ps, $\bullet C_2H_4O^-$ is further reduced by Li^0 and forms Li_2O along with one electron transfer (Figure 3b). In addition to one-electron reduction, two-electron reduction was also observed in the simulation. EC underwent a two-electron reduction to form $CO_3{}^{2-}$ and C_2H_4, as previously observed in an experiment. Further reductions occurred at 50.60 and 56.50 ps, resulting in the formation of Li_2O from $CO_3{}^{2-}$ (Figure 3c).

The decomposition of EMC is slower than EC and generally falls into two categories. As shown in Figure 3d, the C–O bond breaks with Li_2O at 50.6 ps, and then the C–O bond breaks, leading to the formation of CO and CH_3O^- at 55.69 ps. The other reaction path

involves the initial detachment of the $–OCH_3$ group from the carbon chain via a one-electron reduction, followed by the breaking of the C–O bond in the remaining $–OCOCH_2CH_3$ species, yielding CO and $C_2H_5O^-$ (Figure 3e). EMC decomposition did not occur in the first 50 ps of the AIMD simulation but began in the early stages of the HAIR simulation, revealing a similar reaction mechanism.

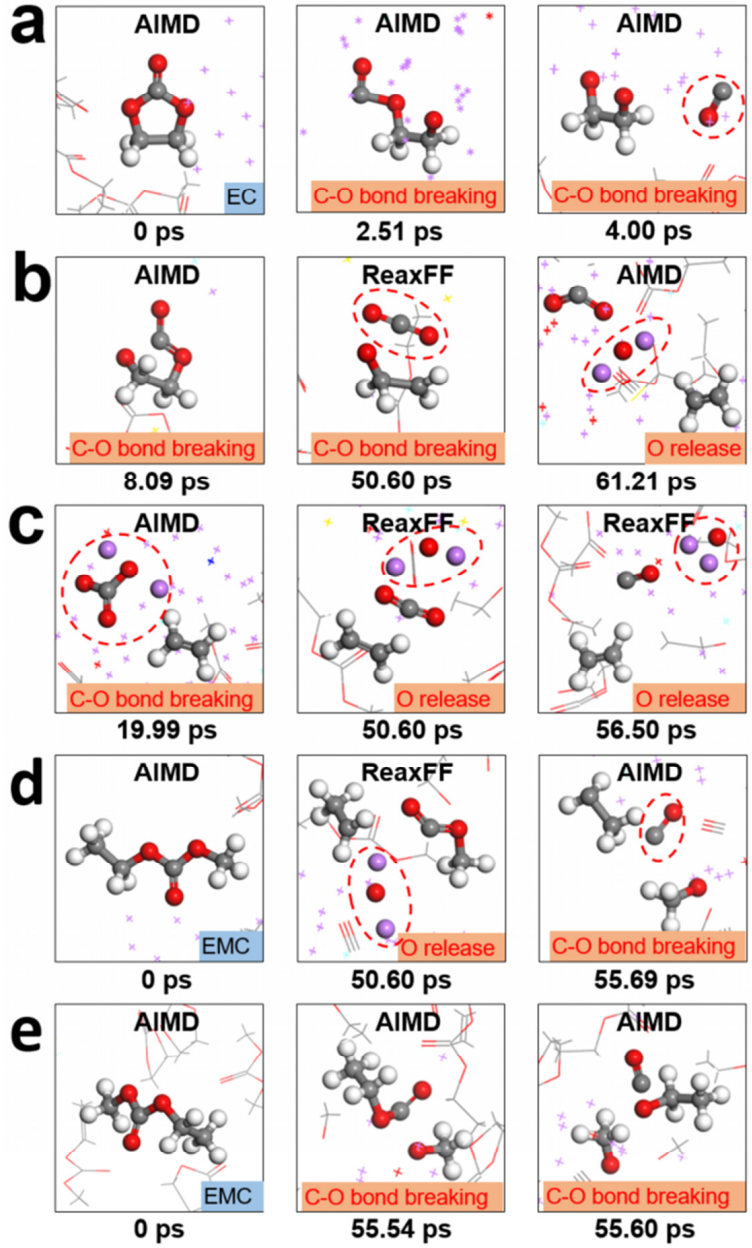

Figure 3. Decomposition pathways of EC and EMC for the 1 M LiDFTFSI-EC/EMC system obtained from AIMD and HAIR simulations between 0 and 61.21 ps. (**a**) Pathway 1 of EC, (**b**) pathway 2 of EC, (**c**) pathway 3 of EC, (**d**) pathway 1 of EMC, and (**e**) pathway 2 of EMC. The color codes are the same as those in Figure 1a.

After the initial decomposition, deeper reactions continue, forming the main products of the SEI. The products and primitive SEI formed after 2.86 ns of the HAIR simulation are shown in Figures S5 and S6. The inner SEI layer, close to the anode surface, predominantly contains inorganic compounds like Li_2O, LiF, etc. [53,54]. These inorganic compounds improve mechanical properties, inhibit lithium dendrite growth, decrease electrolyte consumption, and promote a uniform and stable SEI, thereby potentially enhancing battery

cycle performance. Instead, the outer SEI layer, close to the electrolyte, consists mainly of carbon–oxygen organic compounds from solvent decomposition, consistent with previous experiments [42,43]. To further analyze the products and atomic structure of the SEI, the XPS spectra of C 1 s, O 1 s, and F 1 s were simulated, as shown in Figure 4. C atoms exhibit a complex chemical environment characterized by various bond types, including C–O, C–C, C–H, and C=O bonds (Figure 4a), primarily arising from the decomposition of solvents into RC–O (e.g., CH_3OLi and C_2H_5OLi). In Figure 4b, O atoms are either bonded to C, forming C–O and C=O bonds, which confirm the presence of carbon–oxygen groups and correlate with the C 1 s XPS spectrum, or exist as Li_2O. The schematic diagram of $DFTFSI^-$ and solvent decomposition shows that F atoms bond with Li^+ to form LiF (Figure 4c). The theoretical XPS predictions agree well with the experimental results, demonstrating the reliability of the simulations.

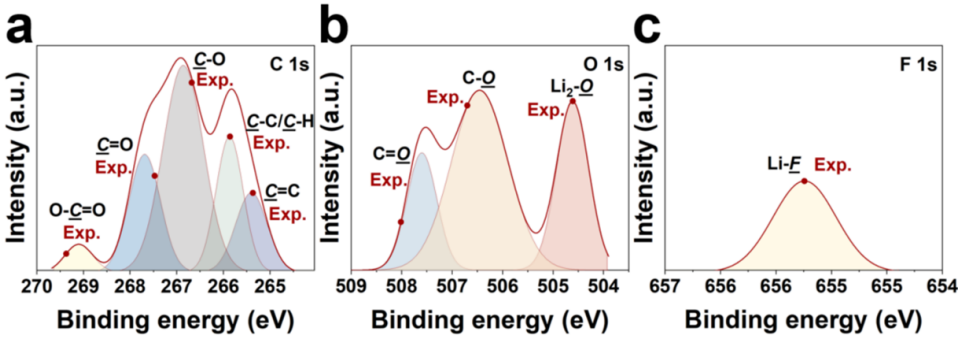

Figure 4. XPS of the LiDFTFSI-EC/EMC system. (**a**) C 1 s, (**b**) O 1 s, and (**c**) F 1 s. The experimental binding energy shifts in C 1 s, O 1 s, and F 1 s are marked with red dots [55–58].

3.3. $DFTFSI^-$ Passivated Al

In lithium batteries, Al is the cathode current collector due to its stability at high potentials, but electrolyte salts can reach and contact Al through electrolyte pervasion. In addition to regulating the anode interphase, LiDFTFSI, as the reactive active component, can remarkably suppress dissolution of the Al^0 current collector at high potentials (>4.2 V vs Li/Li^+) in comparison with LiTFSI. The Al^0 current collector maintains good stability within the battery because Al foil naturally forms a protective Al_2O_3 layer [59]. However, when the voltage exceeds the threshold, Al_2O_3 can be destroyed in the organic solution, exposing fresh Al^0. This leads to progressive corrosion of the Al^0 current collector, which impacts performance and longevity. Oxidative corrosion of Al is a challenge in developing new electrolyte salts [60]. The asymmetric structure of LiDFTFSI and the high reactivity of the $–CF_2H$ group rapidly dissociate to form AlF_3, which then protects the anode. This protective layer helps in passivating the Al^0 current collector, which is crucial for the battery's stability and longevity [61].

To test such a hypothesis, we examined the defluorination process on the $–CF_2H$ group on the Al metal surface, as shown in Figure 5. DFT calculations show that the Gibbs free energy change (ΔG) for this process is −1.64 eV, compared to −0.94 eV for LiTFSI. The results indicate that LiDFTFSI defluorinates more readily on the Al electrode, facilitating the subsequent formation of AlF_3, validating our hypothesis well. Therefore, the protective mechanism of LiDFTFSI on Al foil can be described as follows: LiDFTFSI diffuses and adsorbs onto the Al foil and decomposes, and the resulting F ions react with Al^{3+} to form an AlF_3 passivation layer. This layer prevents further exposure of the Al metal and suppresses interfacial side reactions.

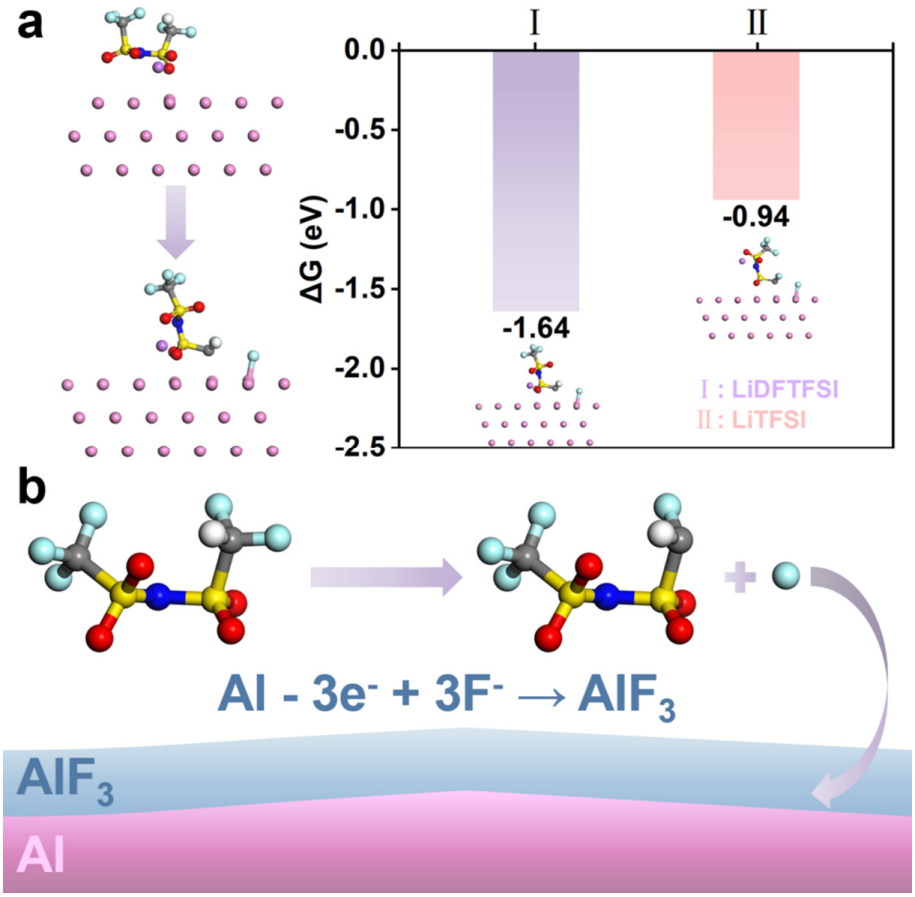

Figure 5. LiDFTFSI defluorination achieves passivation of Al. (**a**) ΔG of defluorination of the lithium salt on the Al (111) surface, and (**b**) a schematic diagram of LiDFTFSI passivating Al. Color codes are the same as in Figure 1a.

4. Conclusions

To summarize, we conducted atomic simulations to investigate how an asymmetric sulfonyl imide salt (LiDFTFSI) influences the microscopic solvation structure and underlying interfacial reaction mechanisms in LMBs. According to cMD simulations, presence of the asymmetric functional group (–CF_2H) increased the proportion of the LAC solvation structure in the LiDFTFSI-EC/EMC system compared to the LiTFSI–based electrolyte, while substantially decreasing the portion of the SSL solvation structure. cMD simulations also suggest that $DFTFSI^-$ has a greater coordination capacity with Li^+, thereby triggering salt-prone interfacial reactions. A HAIR simulation was employed to investigate the initial interface reactions and the detailed SEI generation process of the LiDFTFSI–based electrolyte. A homogeneous and stable SEI layer relying on the substantial production of Li_2O and LiF was formed as a result of the preferred decomposition of LiDFTFSI. The reliability of the HAIR and XPS simulations was confirmed by comparing theoretical XPS simulations of the SEI with actual XPS spectra.

Furthermore, LiDFTFSI tends to defluorinate on the Al surface, facilitating the formation of a passivation layer that suppresses corrosion of the Al^0 current collector, providing a clear explanation of the perplexing experimental observation. This study clearly clarifies the solvation structure and interface chemistry of electrolytes, providing new insights into the design of new electrolytes to enhance the performance of LMBs.

Supplementary Materials: The following supporting information can be downloaded at https://www.mdpi.com/article/10.3390/batteries10060180/s1: Figure S1: The workflow diagram for simulating interfacial reactions; Figure S2: Atomic molecular geometries for anions and solvents and the initial

model for the 1 M LiDFTFSI-EC/EMC system; Figure S3: Examples of three solvation structures of the LiTFSI-EC/EMC electrolyte and the ESP energy diagrams of $DFTFSI^-$ and $TFSI^-$; Figure S4: The experimentally speculated reduction mechanism for LiDFTFSI; Figure S5: The molecular geometries of the final products in the SEI obtained from the 2.8 ns HAIR simulation; Figure S6: Composition and structure of the SEI in the 1 M LiDFTFSI-EC/EMC system for the simulations; Table S1: Li^+ coordination in the LiDFTFSI–based and LiTFSI–based electrolytes. Refs. [43,47,62–64].

Author Contributions: Conceptualization, S.F. and T.C.; validation, T.Y., L.B. and T.C.; formal analysis, S.F.; writing—original draft preparation, S.F.; writing—review and editing, S.F., Y.L. and T.C.; supervision, T.C.; project administration, T.C.; funding acquisition, T.C.; S.F. and T.Y. contributed equally to this work. All authors have read and agreed to the published version of the manuscript.

Funding: This research was funded by the National Key Research and Development Program of China (Grant No. 2022YFB2502200), Suzhou Key Laboratory of Functional Nano & Soft Materials, the Collaborative Innovation Center of Suzhou Nano Science & Technology, the Priority Academic Program Development of Jiangsu Higher Education Institutions (PAPD), the 111 Project, Joint International Research Laboratory of Carbon-Based Functional Materials and Devices, the National Natural Science Foundation of China (Grant No. 22173066, 22303058), and Natural Science Foundation of Jiangsu Province (Grant No. BK20230065, BK20230475).

Data Availability Statement: The data presented in this study are available upon request from the corresponding author.

Conflicts of Interest: The authors declare no conflicts of interest.

References

1. Winter, M.; Barnett, B.; Xu, K. Before Li ion batteries. *Chem. Rev.* **2018**, *118*, 11433–11456. [CrossRef] [PubMed]
2. Larcher, D.; Tarascon, J.M. Towards greener and more sustainable batteries for electrical energy storage. *Nat. Chem.* **2015**, *7*, 19–29. [CrossRef] [PubMed]
3. Lin, D.; Liu, Y.; Cui, Y. Reviving the lithium metal anode for high-energy batteries. *Nat. Nanotechnol.* **2017**, *12*, 194–206. [CrossRef] [PubMed]
4. Dunn, B.; Kamath, H.; Tarascon, J.-M. Electrical energy storage for the grid: A battery of choices. *Science* **2011**, *334*, 928–935. [CrossRef] [PubMed]
5. Kothalawala, V.N.; Suzuki, K.; Nokelainen, J.; Hyvönen, A.; Makkonen, I.; Barbiellini, B.; Hafiz, H.; Tynjälä, P.; Laine, P.; Välikangas, J.; et al. Compton scattering study of strong orbital delocalization in a $LiNiO_2$ cathode. *Phys. Rev. B* **2024**, *109*, 035139–035143. [CrossRef]
6. Kothalawala, V.N.; Sasikala Devi, A.A.; Nokelainen, J.; Alatalo, M.; Barbiellini, B.; Hu, T.; Lassi, U.; Suzuki, K.; Sakurai, H.; Bansil, A. First principles calculations of the optical response of $LiNiO_2$. *Condens. Matter* **2022**, *7*, 54. [CrossRef]
7. Takenaka, N.; Bouibes, A.; Yamada, Y.; Nagaoka, M.; Yamada, A. Frontiers in theoretical analysis of solid electrolyte interphase formation mechanism. *Adv. Mater.* **2021**, *33*, 2100574–2100588. [CrossRef] [PubMed]
8. Xiao, P.; Yun, X.; Chen, Y.; Guo, X.; Gao, P.; Zhou, G.; Zheng, C. Insights into the solvation chemistry in liquid electrolytes for lithium-based rechargeable batteries. *Chem. Soc. Rev.* **2023**, *52*, 5255–5316. [CrossRef] [PubMed]
9. Fu, Y.; Singh, R.; Feng, S.; Li, J.; Xiao, J.; Bao, J.; Xu, Z.; Lu, D. Understanding of low-porosity sulfur electrode for high-energy lithium-sulfur batteries. *Adv. Energy Mater.* **2023**, *13*, 2203386–2203393. [CrossRef]
10. Wang, H.; Yu, Z.; Kong, X.; Kim, S.C.; Boyle, D.T.; Qin, J.; Bao, Z.; Cui, Y. Liquid electrolyte: The nexus of practical lithium metal batteries. *Joule* **2022**, *6*, 588–616. [CrossRef]
11. Li, M.; Wang, C.; Davey, K.; Li, J.; Li, G.; Zhang, S.; Mao, J.; Guo, Z. Recent progress in electrolyte design for advanced lithium metal batteries. *SmartMat* **2023**, *4*, e1185. [CrossRef]
12. Hobold, G.M.; Lopez, J.; Guo, R.; Minafra, N.; Banerjee, A.; Shirley Meng, Y.; Shao-Horn, Y.; Gallant, B.M. Moving beyond 99.9% coulombic efficiency for lithium anodes in liquid electrolytes. *Nat. Energy* **2021**, *6*, 951–960. [CrossRef]
13. Liu, J.; Bao, Z.; Cui, Y.; Dufek, E.J.; Goodenough, J.B.; Khalifah, P.; Li, Q.; Liaw, B.Y.; Liu, P.; Manthiram, A.; et al. Pathways for practical high-energy long-cycling lithium metal batteries. *Nat. Energy* **2019**, *4*, 180–186. [CrossRef]
14. Nanda, S.; Gupta, A.; Manthiram, A. Anode-Free Full Cells: A Pathway to High-energy density lithium-metal batteries. *Adv. Energy Mater.* **2021**, *11*, 2000804. [CrossRef]
15. Jie, Y.; Ren, X.; Cao, R.; Cai, W.; Jiao, S. Advanced liquid electrolytes for rechargeable Li metal batteries. *Adv. Funct. Mater.* **2020**, *30*, 1910777. [CrossRef]
16. Jagger, B.; Pasta, M. Solid electrolyte interphases in lithium metal batteries. *Joule* **2023**, *7*, 2228–2244. [CrossRef]
17. Qi, M.; Xie, L.; Han, Q.; Zhu, L.; Chen, L.; Cao, X. An overview of the key challenges and strategies for lithium metal anodes. *J. Energy Storage* **2022**, *47*, 103641. [CrossRef]

18. Cheng, X.-B.; Zhang, R.; Zhao, C.-Z.; Zhang, Q. Toward safe lithium metal anode in rechargeable batteries: A review. *Chem. Rev.* **2017**, *117*, 10403–10473. [CrossRef]
19. Wang, Q.; Yao, Z.; Zhao, C.; Verhallen, T.; Tabor, D.P.; Liu, M.; Ooms, F.; Kang, F.; Aspuru-Guzik, A.; Hu, Y.-S.; et al. Interface chemistry of an amide electrolyte for highly reversible lithium metal batteries. *Nat. Commun.* **2020**, *11*, 4188. [CrossRef]
20. Zhai, P.; Liu, L.; Gu, X.; Wang, T.; Gong, Y. Interface engineering for lithium metal anodes in liquid electrolyte. *Adv. Energy Mater.* **2020**, *10*, 2001257. [CrossRef]
21. Liu, B.; Zhang, J.-G.; Xu, W. Advancing lithium metal batteries. *Joule* **2018**, *2*, 833–845. [CrossRef]
22. Liu, S.; Ma, Y.; Zhou, Z.; Lou, S.; Huo, H.; Zuo, P.; Wang, J.; Du, C.; Yin, G.; Gao, Y. Inducing uniform lithium nucleation by integrated lithium-rich li-in anode with lithiophilic 3D framework. *Energy Storage Mater.* **2020**, *33*, 423–431. [CrossRef]
23. Wang, X.; Zeng, W.; Hong, L.; Xu, W.; Yang, H.; Wang, F.; Duan, H.; Tang, M.; Jiang, H. Stress-driven lithium dendrite growth mechanism and dendrite mitigation by electroplating on soft substrates. *Nat. Energy* **2018**, *3*, 227–235. [CrossRef]
24. Wang, T.; Zhai, P.; Legut, D.; Wang, L.; Liu, X.; Li, B.; Dong, C.; Fan, Y.; Gong, Y.; Zhang, Q. S-doped graphene-regional nucleation mechanism for dendrite-free lithium metal anodes. *Adv. Energy Mater.* **2019**, *9*, 1804000. [CrossRef]
25. Zhao, J.; Liao, L.; Shi, F.; Lei, T.; Chen, G.; Pei, A.; Sun, J.; Yan, K.; Zhou, G.; Xie, J.; et al. Surface fluorination of reactive battery anode materials for enhanced stability. *J. Am. Chem. Soc.* **2017**, *139*, 11550–11558. [CrossRef] [PubMed]
26. Liu, Y.; Lin, D.; Yuen, P.Y.; Liu, K.; Xie, J.; Dauskardt, R.H.; Cui, Y. An artificial solid electrolyte interphase with high Li-ion conductivity, mechanical strength, and flexibility for stable lithium metal anodes. *Adv. Mater.* **2017**, *29*, 1605531. [CrossRef] [PubMed]
27. Zheng, J.; Engelhard, M.H.; Mei, D.; Jiao, S.; Polzin, B.J.; Zhang, J.-G.; Xu, W. Electrolyte additive enabled fast charging and stable cycling lithium metal batteries. *Nat. Energy* **2017**, *2*, 17012. [CrossRef]
28. Weber, R.; Genovese, M.; Louli, A.J.; Hames, S.; Martin, C.; Hill, I.G.; Dahn, J.R. Long cycle life and dendrite-free lithium morphology in anode-free lithium pouch cells enabled by a dual-salt liquid electrolyte. *Nat. Energy* **2019**, *4*, 683–689. [CrossRef]
29. Pham, T.D.; Bin Faheem, A.; Lee, K.-K. Design of a LiF-rich solid electrolyte interphase layer through highly concentrated LiFSI–THF electrolyte for stable lithium metal batteries. *Small* **2021**, *17*, 2103375. [CrossRef]
30. Jiao, S.; Ren, X.; Cao, R.; Engelhard, M.H.; Liu, Y.; Hu, D.; Mei, D.; Zheng, J.; Zhao, W.; Li, Q.; et al. Stable cycling of high-voltage lithium metal batteries in ether electrolytes. *Nat. Energy* **2018**, *3*, 739–746. [CrossRef]
31. Yu, Z.; Wang, H.; Kong, X.; Huang, W.; Tsao, Y.; Mackanic, D.G.; Wang, K.; Wang, X.; Huang, W.; Choudhury, S.; et al. Molecular design for electrolyte solvents enabling energy-dense and long-cycling lithium metal batteries. *Nat. Energy* **2020**, *5*, 526–533. [CrossRef]
32. Yu, Z.; Rudnicki, P.E.; Zhang, Z.; Huang, Z.; Celik, H.; Oyakhire, S.T.; Chen, Y.; Kong, X.; Kim, S.C.; Xiao, X.; et al. Rational solvent molecule tuning for high-performance lithium metal battery electrolytes. *Nat. Energy* **2022**, *7*, 94–106. [CrossRef]
33. Zhang, X.-Q.; Cheng, X.-B.; Chen, X.; Yan, C.; Zhang, Q. Fluoroethylene carbonate additives to render uniform Li deposits in lithium metal batteries. *Adv. Funct. Mater.* **2017**, *27*, 1605989. [CrossRef]
34. Hou, T.; Yang, G.; Rajput, N.N.; Self, J.; Park, S.-W.; Nanda, J.; Persson, K.A. The influence of FEC on the solvation structure and reduction reaction of $LiPF_6$/EC electrolytes and its implication for solid electrolyte interphase formation. *Nano Energy* **2019**, *64*, 103881. [CrossRef]
35. Wang, X.; Wang, S.; Wang, H.; Tu, W.; Zhao, Y.; Li, S.; Liu, Q.; Wu, J.; Fu, Y.; Han, C.; et al. Hybrid electrolyte with dual-anion-aggregated solvation sheath for stabilizing high-voltage lithium-metal batteries. *Adv. Mater.* **2021**, *33*, 2007945. [CrossRef]
36. Fu, J.; Ji, X.; Chen, J.; Chen, L.; Fan, X.; Mu, D.; Wang, C. Lithium nitrate regulated sulfone electrolytes for lithium metal batteries. *Angew. Chem. Int. Ed.* **2020**, *59*, 22194–22201. [CrossRef]
37. Yang, F.; Wang, P.; Huang, Q.; Luo, J.; Hu, R.; Huang, Q.; Mao, C.; Yang, L.; Liang, G.; Li, Y.; et al. Saccharin sodium coupling fluorinated solvent enabled stable interface for high--voltage Li-metal batteries. *Small* **2024**, e2311961. [CrossRef] [PubMed]
38. Kwon, H.; Lee, J.; Roh, Y.; Baek, J.; Shin, D.; Yoon, J.; Ha, H.; Kim, J.; Kim, H. An electron-deficient carbon current collector for anode-free li-metal batteries. *Nat. Commum.* **2021**, *12*, 5537–5549. [CrossRef]
39. Mäntymäki, M.; Ritala, M.; Leskelä, M. Metal fluorides as lithium-ion battery materials: An atomic layer deposition perspective. *Coatings* **2018**, *8*, 277–316. [CrossRef]
40. Xu, K. Nonaqueous liquid electrolytes for lithium-based rechargeable batteries. *Chem. Rev.* **2004**, *104*, 4303–4418. [CrossRef]
41. Wang, S.; Qiu, W.; Guan, Y.; Yu, B.; Zhao, H.; Liu, W. Electrochemical characteristics of $LiM_xFe_{1-x}PO_4$ cathode with LiBOB based electrolytes. *Electrochim. Acta* **2007**, *52*, 4907–4910. [CrossRef]
42. Zhang, H.; Oteo, U.; Judez, X.; Eshetu, G.G.; Martinez-Ibañez, M.; Carrasco, J.; Li, C.; Armand, M. Designer anion enabling solid-state lithium-sulfur batteries. *Joule* **2019**, *3*, 1689–1702. [CrossRef]
43. Qiao, L.; Oteo, U.; Martinez-Ibañez, M.; Santiago, A.; Cid, R.; Sanchez-Diez, E.; Lobato, E.; Meabe, L.; Armand, M.; Zhang, H. Stable non-corrosive sulfonimide salt for 4-V-class lithium metal batteries. *Nat. Mater.* **2022**, *21*, 455–462. [CrossRef] [PubMed]
44. Liu, Y.; Yu, P.; Wu, Y.; Yang, H.; Xie, M.; Huai, L.; Goddard, W.A., III; Cheng, T. The DFT-ReaxFF hybrid reactive dynamics method with application to the reductive decomposition reaction of the TFSI and DOL electrolyte at a lithium-metal anode surface. *J. Phys. Chem. Lett.* **2021**, *12*, 1300–1306. [CrossRef] [PubMed]
45. Abraham, M.J.; Murtola, T.; Schulz, R.; Páll, S.; Smith, J.C.; Hess, B.; Lindahl, E. GROMACS: High performance molecular simulations through multi-level parallelism from laptops to supercomputers. *SoftwareX* **2015**, *1–2*, 19–25. [CrossRef]

46. Kresse, G.; Joubert, D. From ultrasoft pseudopotentials to the projector augmented-wave method. *Phys. Rev. B* **1999**, *59*, 1758–1775. [CrossRef]
47. Perdew, J.P.; Burke, K.; Ernzerhof, M. Generalized gradient approximation made simple. *Phys. Rev. B* **1996**, *77*, 3865–3868. [CrossRef] [PubMed]
48. Grimme, S.; Ehrlich, S.; Goerigk, L. Effect of the damping function in dispersion corrected density functional theory. *J. Comput. Chem.* **2011**, *32*, 1456–1465. [CrossRef]
49. Qi, F.; Yu, P.; Zhou, Q.; Liu, Y.; Sun, Q.; Ma, B.; Ren, X.; Cheng, T. Preferential decomposition of the major anion in a dual-salt electrolyte facilitates the formation of organic-inorganic composite solid electrolyte interphase. *J. Chem. Phys.* **2023**, *158*, 104704. [CrossRef]
50. Chen, Y.; He, Q.; Zhao, Y.; Zhou, W.; Xiao, P.; Gao, P.; Tavajohi, N.; Tu, J.; Li, B.; He, X.; et al. Breaking solvation dominance of ethylene carbonate via molecular charge engineering enables lower temperature battery. *Nat. Commun.* **2023**, *14*, 8326. [CrossRef]
51. Cheng, H.; Sun, Q.; Li, L.; Zou, Y.; Wang, Y.; Cai, T.; Zhao, F.; Liu, G.; Ma, Z.; Wahyudi, W.; et al. Emerging era of electrolyte solvation structure and interfacial model in batteries. *ACS Energy Lett.* **2022**, *7*, 490–513. [CrossRef]
52. Liu, Y.; Wu, Y.; Sun, Q.; Ma, B.; Yu, P.; Xu, L.; Xie, M.; Yang, H.; Cheng, T. Formation of linear oligomers in solid electrolyte interphase via two-electron reduction of ethylene carbonate. *Adv. Theory Simul.* **2022**, *5*, 2100612. [CrossRef]
53. Zhao, Q.; Stalin, S.; Archer, L.A. Stabilizing metal battery anodes through the design of solid electrolyte interphases. *Joule* **2021**, *5*, 1119–1142. [CrossRef]
54. Gong, C.; Pu, S.D.; Gao, X.; Yang, S.; Liu, J.; Ning, Z.; Rees, G.J.; Capone, I.; Pi, L.; Liu, B.; et al. Revealing the role of fluoride-rich battery electrode interphases by operando transmission electron microscopy. *Adv. Energy Mater.* **2021**, *11*, 2003118. [CrossRef]
55. Stephan, A.M.; Prem Kumar, T.; Thomas, S.; Bongiovanni, R.; Nair, J.R.; Angulakshmi, N.; Pollicino, A. $Ca_3(PO_4)_2$-incorporated poly(ethylene oxide)-based nanocomposite electrolytes for lithium batteries. Part II. Interfacial properties investigated by XPS and a.c. impedance studies. *J. Appl. Polym. Sci.* **2012**, *124*, 3255–3263. [CrossRef]
56. Schulz, N.; Hausbrand, R.; Dimesso, L.; Jaegermann, W. XPS-Surface Analysis of SEI layers on Li-ion cathodes: Part I. Investigation of initial surface chemistry. *J. Electrochem. Soc.* **2018**, *165*, A819. [CrossRef]
57. Rustomji, C.S.; Yang, Y.; Kim, T.K.; Mac, J.; Kim, Y.J.; Caldwell, E.; Chung, H.; Meng, Y.S. Liquefied gas electrolytes for electrochemical energy storage devices. *Science* **2017**, *356*, eaal4263. [CrossRef] [PubMed]
58. Fang, D.; He, F.; Xie, J.; Xue, L. Calibration of binding energy positions with C1s for XPS results. *J. Wuhan Univ. Technol. Mater. Sci. Ed.* **2020**, *35*, 711–718. [CrossRef]
59. Yang, S.; Zhong, J.; Li, S.; Li, B. Revisiting aluminum current collector in lithium-ion batteries: Corrosion and countermeasures. *J. Energy Chem.* **2024**, *89*, 610–634. [CrossRef]
60. Ma, T.; Xu, G.; Li, Y.; Wang, L.; He, X.; Zheng, J.; Liu, J.; Engelhard, M.; Zapol, P.; Curtiss, L.; et al. Revisiting the corrosion of the aluminum current collector in lithium-ion batteries. *J. Phys. Chem. Lett.* **2017**, *8*, 1072–1077. [CrossRef]
61. Rodríguez, S.; Candia, A.; Stankovic, I.; Passeggi, M.; Ruano, G. Study of in-plane and interlayer interactions during aluminum fluoride intercalation in graphite: Implications for the development of rechargeable batteries. *ACS Appl. Nano Mater.* **2023**, *6*, 16977–16985. [CrossRef]
62. Köhler, L.; Kresse, G. Density functional study of CO on Rh(111). *Phys. Rev. B* **2004**, *70*, 165405. [CrossRef]
63. Yang, H.; Negreiros, F.R.; Sun, Q.; Xie, M.; Sementa, L.; Stener, M.; Ye, Y.; Fortunelli, A.; Goddard, W.A., III; Cheng, T. Predictions of chemical shifts for reactive intermediates in CO_2 reduction under operando conditions. *ACS Appl. Mater. Interfaces* **2021**, *13*, 31554–31560. [CrossRef]
64. Qian, J.; Baskin, A.; Liu, Z.; Prendergast, D.; Crumlin, E.J. Addressing the sensitivity of signals from solid/liquid ambient pressure XPS (APXPS) measurement. *J. Chem. Phys.* **2020**, *153*, 044709. [CrossRef] [PubMed]